Structural and Biochemical Analyses of Shikimate Dehydrogenase AroE from *Aquifex aeolicus*: Implications for the Catalytic Mechanism[†,‡]

Jianhua Gan,[§,⊥] Yan Wu,[§,#] Ponraj Prabakaran,[||,⊥,#] Yijun Gu,[||,⊥] Yue Li,[||,#] Michelle Andrykovitch,[||,⊥] Hehua Liu,[⊥] Yunchen Gong,[#] Honggao Yan,*[,#] and Xinhua Ji*[,⊥]

Center for Cancer Research, National Cancer Institute, Frederick, Maryland 21702, and Department of Biochemistry and Molecular Biology, Michigan State University, East Lansing, Michigan 48824

Received December 19, 2006; Revised Manuscript Received May 22, 2007

ABSTRACT: The shikimate biosynthetic pathway is essential to microorganisms, plants, and parasites but absent from mammals. Therefore, shikimate dehydrogenase (SD) and other enzymes in the pathway are attractive targets for developing nontoxic antimicrobial agents, herbicides, and antiparasite drugs. SD catalyzes the fourth reaction in the pathway, the nicotinamide adenine dinucleotide phosphate- (NADP-) dependent reduction of 3-dehydroshikimic acid to shikimic acid (SA), as well as its reverse, by the transfer of a hydride. Previous structural studies reveal that the enzyme exists in two major conformations, an open and a closed form. For the reaction to occur, it is believed that the catalytic complex assumes the closed conformation. Nonetheless, the only structure containing both SA and $NADP^+$ exhibits an open conformation (PDB entry 2EV9). Here, we present two crystal structures of *Aquifex aeolicus* SD, including a ternary complex with both SA and $NADP^+$, which assumes the closed conformation and therefore contains a catalytically competent active site. On the basis of preexisting and novel structural and biochemical data, a catalytic mechanism is proposed.

The shikimate pathway is a biosynthetic route leading to the synthesis of aromatic amino acids, folate cofactors, ubiquinone, and many secondary metabolites (*1*, *2*). The pathway is essential to algae, plants, bacteria, fungi, and parasites, whereas it is absent from mammals (*2*, *3*). Therefore, it is a target for the development of nontoxic antimicrobial agents (*4*), herbicides (*3*, *5*), and antiparasite drugs (*6*, *7*). In addition, the pathway has been used for industrial production of hydroaromatic intermediates (*8*, *9*).

The shikimate pathway contains seven reactions each catalyzed by an enzyme, including 3-deoxy-D-*arabino*-heptulosonate-7-phosphate synthase, 3-dehydroquinate synthase, 3-dehydroquinase, shikimate dehydrogenase (SD),[1] shikimate kinase, 5-enolpyruvylshikimate 3-phosphate synthase, and chorismate synthase. Three-dimensional structures are available for representatives of all seven enzymes. 5-Enolpyruvylshikimate 3-phosphate synthase has been an effective target for the development of nontoxic herbicide glyphosate (*10*). However, after more than 20 years of extensive usage, glyphosate-resistant weeds have recently emerged (*11*, *12*), underlining the importance of target diversity.

To date, three classes of SD have been identified and characterized, AroE, YdiB, and SD-like proteins (SD-L). AroE (EC 1.1.1.25) catalyzes the fourth reaction in the shikimate pathway, the nicotinamide adenine dinucleotide phosphate- (NADP-) dependent reduction of 3-dehydroshikimic acid (DHSA) to shikimic acid (SA) (Figure 1A). YdiB (EC 1.1.1.282) is a bifunctional enzyme; it also catalyzes the reversible reduction of dehydroquinate to quinate in the presence of NAD (nicotinamide adenine dinucleotide). SD-L catalyzes the oxidation of SA only but with an ∼1000-fold lower rate when compared with that of AroE (*13*, *14*).

Since 2003, a total of 14 crystal structures of SD have been reported, including PDB (*15*) entries 1NPD (*16*), 1O9B and 1NYT (*13*), 1NVT (*17*), 1P74 and 1P77 (*18*), 1NPY (*14*), 1VI2 (*19*), 2GPT (*20*), and 1WXD, 2CY0, 2D5C, 2EV9, and 2NLO (primary citation not available). These structures have revealed the highly conserved overall architecture of these enzymes, featuring (i) the general fold of the polypeptide chain, the N-terminal catalytic domain containing a unique α/β fold and the C-terminal NAD(P)-binding domain comprising the Rossmann fold, (ii) two distinct conformations of the overall structure, an open form and a closed form, (iii) the protein−NAD(P) and protein−

[†] This research was supported by NIH Grant GM51901 and MSU Center of Excellence Fund (to H.Y.) and the Intramural Research Program of the NIH, National Cancer Institute, Center for Cancer Research.

[‡] The coordinates and structure factors have been deposited with the Protein Data Bank, Research Collaboratory for Structural Bioinformatics, Rutgers University, New Brunswick, NJ (http://www.rcsb.org/). The accession codes are 2HK8 (for apo-AaSD) and 2HK9 (for AaSD·$NADP^+$·SA).

* To whom correspondence should be addressed. Telephone: 517-353-5282 (H.Y.); 301-846-5035 (X.J.). Fax: 517-353-9334 (H.Y.); 301-846-6073 (X.J.). E-mail: yanh@pilot.msu.edu (H.Y.); jix@ncifcrf.gov (X.J.).

[§] These authors contributed equally to this work.

[||] These authors contributed equally to this work.

[⊥] National Cancer Institute.

[#] Michigan State University.

[1] Abbreviations: SA, shikimic acid; DHSA, 3-dehydroshikimic acid; SD, shikimate dehydrogenase; AroE, shikimate dehydrogenase AroE; SD-L, shikimate dehydrogenase-like protein; YdiB, shikimate/quinate dehydrogenase YdiB; AaSD, *Aquifex aeolicus* shikimate dehydrogenase AroE; TtSD, *Thermus thermophilus* shikimate dehydrogenase AroE; NADP, nicotinamide adenine dinucleotide phosphate; RMSD, root-mean-square deviation.

10.1021/bi602601e CCC: $37.00
Published on Web 07/25/2007

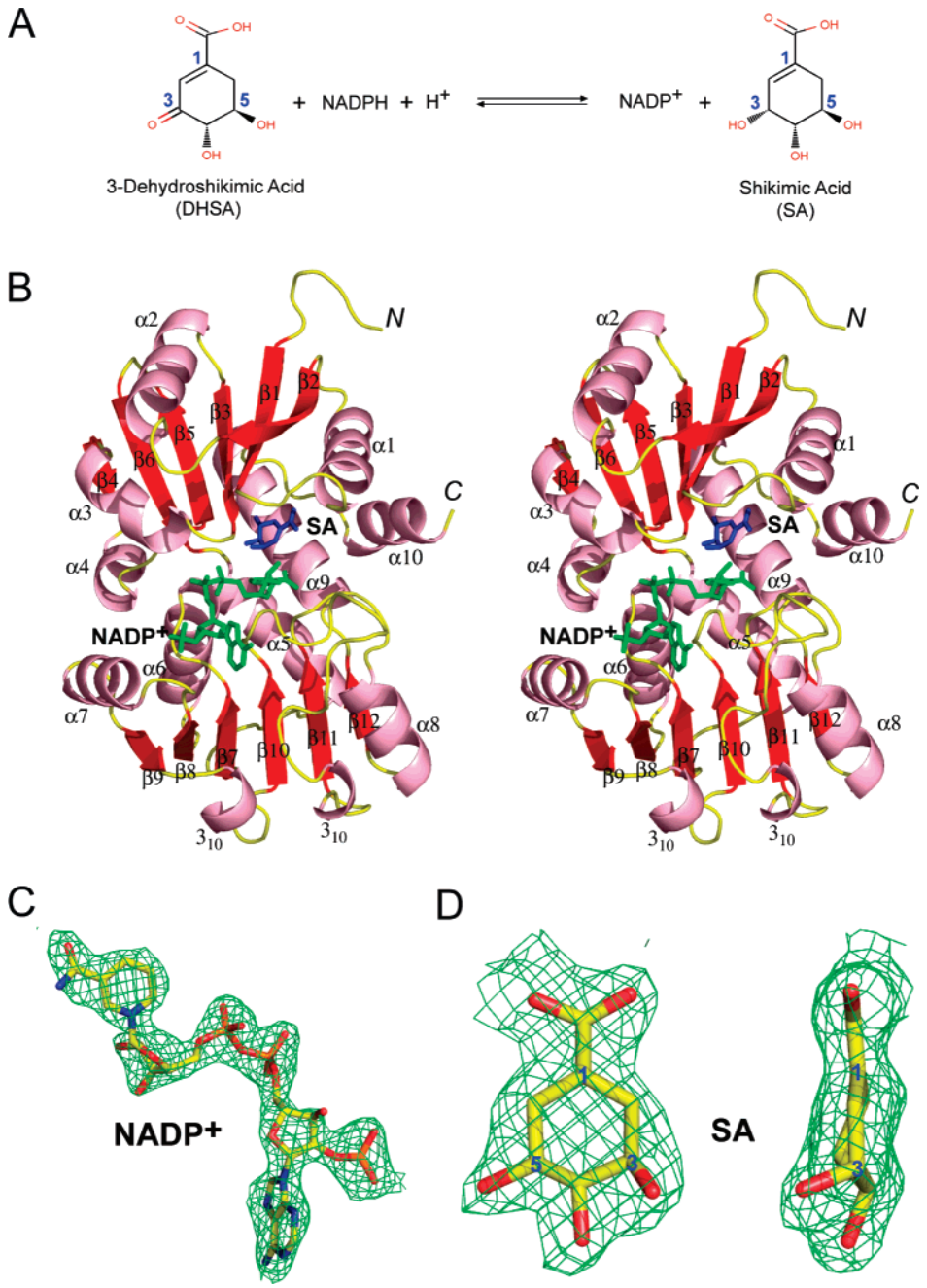

FIGURE 1: Reaction and structure of AaSD. (A) The reversible reaction catalyzed by AaSD. (B) Stereoview showing the overall structure of the AaSD·NADP$^+$·SA complex. Secondary structure elements are indicated by pink spirals for α-helices, red arrows for β-strands, and yellow pipes for loops. The NADP$^+$ and SA molecules are shown as stick models in green and blue, respectively. The composite annealed omit maps ($2F_o - F_c$, contoured at the 1.0σ level) are shown for the enzyme-bound NADP$^+$ (C) and SA (D) molecules. The two views of SA are related by a 90° rotation around the vertical axis, showing the half-chair conformation of the ring system and the tetrahedral (sp^3) geometry of C3.

SA interactions, and (iv) conserved active site residues K70 and D106 [residue numbers in *Aquifex aeolicus* SD AroE (AaSD)], which are hydrogen bonded to the hydroxyl groups of SA. It is intriguing that in vitro data have shown that the two conserved residues play distinct roles in these enzymes: they are key catalytic groups in AroE (*20*) and SD-L (*14*) but are important only for substrate binding in YdiB (*21*).

To elucidate the catalytic mechanisms of AroE, YdiB, and SD-L, catalytically competent ternary complexes of each class containing both a cofactor and a substrate are critical. Among the 14 structures, however, only a *Thermus thermophilus* SD AroE (TtSD) structure contains both NADP$^+$ and SA (TtSD·NADP$^+$·SA, 2EV9). Unfortunately, this ternary complex exhibits the open conformation with an exposed active site, in which the redox reaction is not likely to occur. Here, we present the results of our biochemical analysis and two crystal structures of AaSD. Our structure of the ternary AaSD·NADP$^+$·SA complex has the closed conformation with a catalytically competent active center and, therefore, provides critical insight into the mechanism of AroE-catalyzed hydride transfer.

EXPERIMENTAL PROCEDURES

Cloning, Expression, and Purification. We expressed the AaSD in two forms, wild type and His tagged. For the wild

type, the gene for AaSD was amplified by PCR from the genomic DNA of *A. aeolicus* kindly provided by Dr. Ronald V. Swanson of Diversa Corp. and cloned into the expression vector pET-17b (Novagen) by standard recombinant DNA methods. The forward and reverse primers for the PCR amplification were 5′-GGAATTCATATGATTAACGCCCAAACGCAGCTATACGGAG-3′ and 5′-CGGAATTCTTACCCACGGAGATCTCTTACAGATCTTTCTGC-3′, respectively. The coding sequence was verified by DNA sequencing. The *Escherichia coli* strain BL21(DE3) containing the expression construct pET-17b-AaSD was used to produce AaSD. The cells were grown overnight without IPTG induction, harvested by centrifugation, resuspended in 20 mM Tris-HCl buffer (pH 7.5), and broken with a French press. The lysate was centrifuged at ~27000*g* for 20 min. The supernatant was heated to 65 °C for 30 min, centrifuged again, and loaded on to a DEAE-cellulose column linked to an Affi-Gel Blue column both equilibrated with the Tris buffer. The Affi-Gel Blue column was washed with the Tris buffer until OD_{280} = ~0.05 and then eluted with a linear 0−1.0 M NaCl gradient in the same buffer. The fractions containing AaSD were identified by SDS−PAGE. The pure fractions were concentrated with an Amicon cell using a YM10 membrane, dialyzed against the buffer containing 1 mM HEPES (pH 7.5) and 100 mM NaCl, and lyophilized.

For the His-tagged protein, the AaSD gene was cloned into a modified pET-17b vector to generate an AaSD with a six histidine tag at the N-terminus. The protein was first purified with an Affi-Gel Blue column as described above but without the heating step and DEAE-cellulose precolumn. The Affi-Gel Blue column was eluted with a linear 0−1.5 M NaCl gradient in the Tris buffer. The AaSD fractions from the Affi-Gel Blue column were loaded onto a Ni-NTA column equilibrated with 50 mM phosphate, 300 mM NaCl, and 10 mM imidazole (pH 8.0). The Ni-NTA column was washed with 20 mM imidazole in the phosphate buffer and eluted with 250 mM imidazole in the same buffer. The pure His-tagged AaSD fractions were concentrated, dialyzed, and lyophilized as described for the non-His-tagged AaSD.

Biochemical Analysis. Kinetic measurements were carried out at 25 °C in a buffer consisting of 100 mM Tris-HCl, 100 mM MES, and 100 mM NaCl, which was designed for minimizing the variation of ionic strength for the determination of the pH profile of the kinetic parameters. The reaction was followed by monitoring the formation of NADPH and DHSA spectrophotometrically at 340 nm using an extinction coefficient of 6.22 mM^{-1} cm^{-1}. The SD activity was usually assayed at pH 9.0 under the initial velocity conditions. For the determination of the K_m of SA ($K_{m(SA)}$), $NADP^+$ was fixed at 1 mM and SA was varied from 0.008 to 0.3 mM. For the determination of the K_m of $NADP^+$ ($K_{m(NADP)}$), SA was fixed at 2 mM and $NADP^+$ was varied from 0.004 to 0.18 mM. For the determination of the pH profile of the kinetic parameters, $NADP^+$ was fixed at 1 mM and SA was varied generally in the range of 0.5 $K_{m(SA)}$ to ~10 $K_{m(SA)}$. Kinetic constants were obtained by nonlinear regression analysis of the kinetic data using the program Origin (OriginLab, Northampton, MA) and the Michaelis−Menten equation:

$$v = V_{max}[S]/(K_m + [S]) \quad (1)$$

The pH profile of k_{cat} was fitted with a model that requires a single ionizable group deprotonated for activity (eq 2), and the pH profile of k_{cat}/K_m was fitted with a model that requires two ionizable groups, one deprotonated and the other protonated (eq 3):

$$k_{cat} = \frac{k^\circ_{cat}}{1 + 10^{-pH}/10^{-pK_a}} \quad (2)$$

$$\frac{k_{cat}}{K_m} = \frac{(k_{cat}/K_m)^\circ}{1 + 10^{-pH}/10^{-pK_{a1}} + 10^{-pK_{a2}}/10^{-pH}} \quad (3)$$

where ° indicates the limiting value of k_{cat} or K_m and other symbols have their usual meanings.

Crystallization and X-ray Diffraction Data Collection. Crystals of native (apo-AaSD) and its Hg derivative (AaSD·Hg) were obtained with non-His-tagged protein, whereas the ternary complex (AaSD·$NADP^+$·SA) crystals were obtained with His-tagged AaSD.

Before crystallization, non-His-tagged AaSD was dialyzed for 4 h in 30 mM Tris-HCl (pH 7.5) and 500 mM NaCl, concentrated to 16.3 mg/mL, and injected into a Superdex 75 10/30 column (Pharmacia). The column was calibrated using a SEC molecular weight standard kit from Bio-Rad, and the calibration data were fit to a straight line with $r^2 > 0.999$. The sample was eluted using the same buffer, and the collected fraction was concentrated to a final concentration of 10 mg/mL. Single crystals were grown with the hanging drop vapor diffusion technique at well-controlled room temperature (19 ± 1 °C). The precipitant (well) solution contained 12% PEG 20000 in 0.1 M MES (pH 6.4−6.6). The drops contained equal volumes of the protein and the well solutions. The AaSD·Hg crystal was obtained via soaking an apo-AaSD crystal in the mother liquid containing 0.1 mM ethyl mercuric phosphate for 24 h. Both the native and the HgMAD data were collected at Beamline X9B of the National Synchrotron Light Source at Brookhaven National Labortory, using an ADSC Quantum 4 CCD detector. During data collection, the crystal was kept frozen at 100 K with an Oxford cryocooling system. The cryocondition was 24−25% PEG 400. The derivative crystal was too small to provide a fluorescent spectrum; four recommended wavelengths for HgMAD data collection were used (*22*).

The AaSD·$NADP^+$·SA crystal was grown from hanging drops, each being created by mixing 3.0 μL of protein solution (20 mg/mL His-tagged AaSD, 5.0 mM $NADP^+$, and 5.0 mM SA in 20 mM Tris-HCl, pH 7.2) and 1.0 μL of well solution (0.2 M ammonium acetate and 30% w/v PEG 4000 in 0.1 M sodium acetate, pH 4.6). X-ray diffraction data were collected at the Southeast Regional Collaborative Access Team (SER-CAT) insertion device beamline 22-ID of the Advanced Photon Source (APS) at Argonne National Laboratory.

Data processing was carried out with HKL2000 (*23*). Crystal data and processing statistics are summarized in Table 2. Further data processing was carried out with CCP4 program suite (*24*) for structure solution and refinement.

Structure Solution and Refinement. Four Hg sites were obtained using the program SOLVE (*25*) at 2.5 Å resolution. The heavy atom parameters were refined, and phase im-

Table 1: Structure Refinement Statistics

	apo-AaSD	AaSD·NADP$^+$·SA
resolution (Å)	2.35	2.20
data used for refinement	71656	47090
data used for *R*-free calculations	3638	2364
final *R*-factor[a]	0.213	0.207
final *R*-free	0.265	0.271
no. of amino acid residues/atoms	2125/16797	1284/8444
no. of water oxygens	639	204
no. of NADP$^+$	0	4
no. of SA	0	4
RMSD		
bond distances (Å)	0.008	0.007
bond angles (deg)	1.3	1.3
Ramachandran plot		
residues in most favored region (%)	93.7	89.5
residues in disallowed region (%)	0.0	0.0

[a] Crystallographic *R*-factor $= \sum_{hkl}||F_o| - |F_c||/\sum_{hkl}|F_o|$.

provement with solvent flipping was carried out using the program SHARP (*26*), resulting in an electron density map with recognizable secondary structure elements. The crystal structures of *E. coli* YdiB (PDB entries 1NPD and 1O9B) facilitated model building although the molecular replacement attempts using the two structures as search models were not successful. Both the apo-AaSD and AaSD·NADP$^+$·SA structures were solved with the molecular replacement program PHASER (*27*) using the AaSD·Hg structure (PDB entry 2HK7) as the search model after the Hg atoms and solvent molecules were removed.

The refinement was done with CNS (*28*). Bulk solvent correction was employed. During the refinement, the $2F_o - F_c$ and $F_o - F_c$ electron density maps were regularly inspected and compared with the initial electron density map from HgMAD phasing. Solvent molecules, as peaks ≥ 3.0 on the $F_o - F_c$ map with reasonable hydrogen bond network, were included as water molecules at the later stage of the refinement and verified with omit maps. During the refinement, only weak noncrystallographic symmetry restraints were applied to the Cα atoms of the eight molecules in the apo-AaSD structure. Approximately 5% reflections were randomly selected for *R*-free calculations throughout the refinement. All graphics work was carried out with O (*29*). The refined structures were assessed with PROCHECK (*30*) and WHAT IF (*31*). Illustrations were prepared with MOLSCRIPT (*32*) and PyMOL (*33*).

RESULTS AND DISCUSSION

Sequence of AaSD. DNA sequencing indicates that residue 195 is a Glu and residue 233 is a Leu. These two residues are different from those in the database, in which residue 195 is a Lys and residue 233 is a Phe (Swiss-Prot entry 067049). We believe that these differences are due to errors in the genomic sequencing because (i) we have sequenced several independent clones from different PCR reactions and the results are consistent, (ii) the DNA polymerase used in our cloning work has high fidelity, and (iii) the new identities of the two residues are confirmed by electron density (difference map) during crystal structure determination. These two residues are more than 17 Å away from the catalytic site, and therefore their identities should not have significant influence on catalysis.

Structures of Apo-AaSD and AaSD·NADP$^+$·SA. The statistics for the two structures are summarized in Table 1. There are eight and four crystallographically independent AaSD molecules in the asymmetric unit of apo-AaSD and AaSD·NADP$^+$·SA, respectively. The apo-AaSD structure contains 2125 amino acids (residues 1−266 for molecules A, B, D, E, G, and H, residues 1−265 for molecule C, and residues 1−264 for molecule F) and 639 water molecules. The AaSD·NADP$^+$·SA structure contains 1068 amino acids (residues 1−269 for molecule A, residues 1−267 for molecules B, and residues 1−266 for molecules C and D), four NADP$^+$ molecules (except that the nicotinamide and ribose moieties of NADP$^+$ associated with molecule A are disordered and therefore not included), four SA molecules, assuming an identical half-chair conformation with a 3*R*,4*S*,5*R* arrangement, and 204 water molecules.

The overall structure of molecule D in the AaSD·NADP$^+$·SA structure is illustrated, and the electron density ($2F_o - F_c$ composite annealed omit map contoured at 1.0σ) for the two ligands is shown (Figure 1). The polypeptide chain folds into two domains, an NADP-binding domain and a catalytic domain. The NADP-binding domain, composed of amino acid residues 106−241, belongs to the superfamily of NAD(P)-binding, Rossmann-fold-containing domains. It features a six-stranded parallel β-sheet (β9, β8, β7, β10, β11, and

Table 2: Crystal Data and X-ray Data Collection Statistics

	AaSD·Hg				apo-AaSD	AaSD·NADP$^+$·SA
wavelength (Å)	0.9918 (remote)	1.0072 (peak)	1.0084 (edge 1)	1.0087 (edge 2)		
resolution (Å)	2.5	2.5	2.5	2.5	2.35	2.2
space group	$P2_12_12_1$	$P2_12_12_1$	$P2_12_12_1$	$P2_12_12_1$	*P*1	$P2_12_12_1$
cell dimensions						
a (Å)	36.2	36.2	36.2	36.2	37.4	72.0
b (Å)	74.9	74.9	75.0	75.0	74.0	119.8
c (Å)	190.0	189.9	190.2	190.2	192.1	128.9
α (deg)	90	90	90	90	94.6	90
β (deg)	90	90	90	90	94.2	90
γ (deg)	90	90	90	90	91.8	90
completeness (%), overall (last shell)[a]	94.4 (82.9)	94.4 (82.9)	93.6 (80.4)	93.3 (83.0)	87.2 (44.8)	83.9 (54.5)
redundancy	3.4	3.6	3.6	3.2	2.0	2.9
$I/\sigma(I)$, overall (last shell)	14.8 (2.0)	19.4 (3.1)	17.0 (2.8)	14.0 (1.8)	6.0 (2.4)	8.8 (2.1)
$R_{scaling}$[b] (%), overall (last shell)	8.4 (50.7)	6.5 (34.8)	7.8 (43.5)	7.9 (53.1)	6.6 (27.5)	10.9 (33.1)

[a] The last shell of X-ray diffraction data for AaSD·Hg ($\lambda 1-\lambda 4$), native AaSD, and AaSD·NADP$^+$·SA is 2.59−2.50, 2.43−2.35, and 2.28−2.20 Å, respectively. [b] $R_{scaling} = \sum|I - \langle I\rangle|/\sum I$.

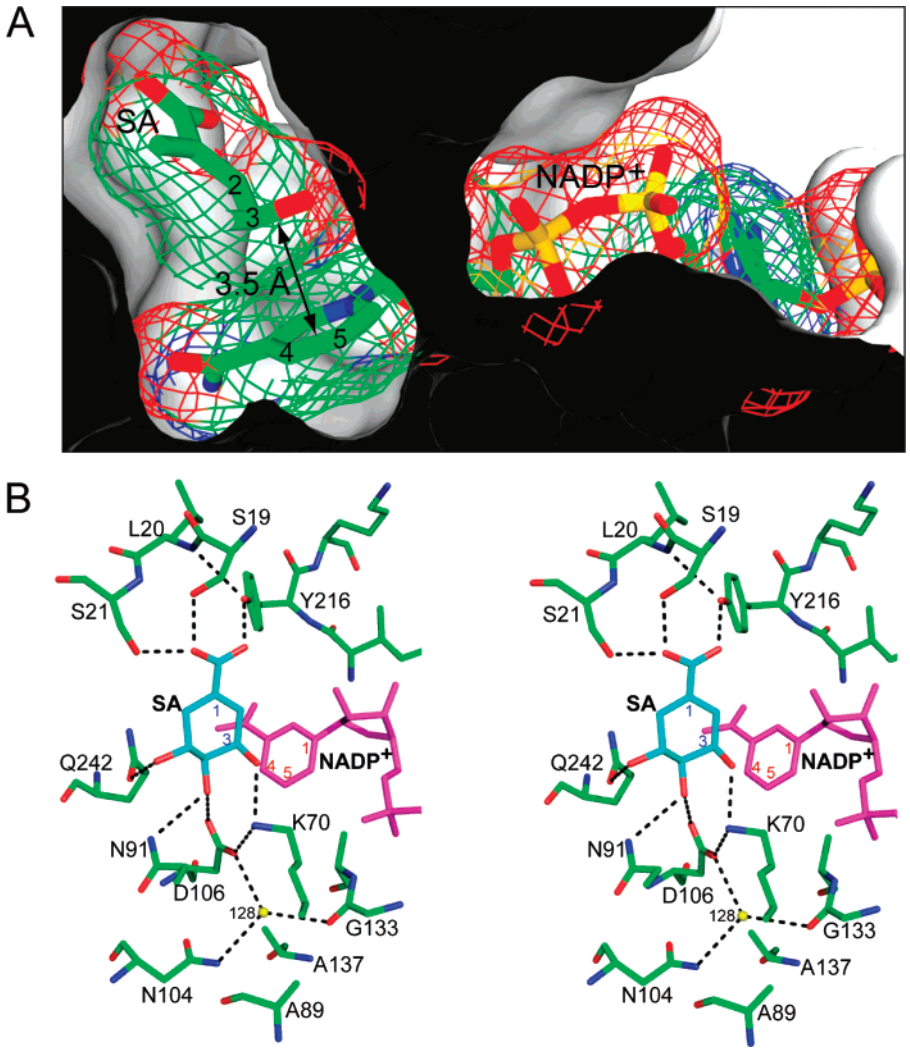

FIGURE 2: SA binding by AaSD and its interaction with $NADP^+$. (A) Clipped view into the active site of AaSD showing the contacting distance (3.5 Å) between SA and the nicotinamide moiety of $NADP^+$ as observed in the AaSD·$NADP^+$·SA structure. The ligands are shown as stick models in atomic color scheme (C, green; O, red; N, blue; and P, orange) and outlined with a mesh representation at van der Waals radii of atoms. The protein is illustrated as a gray surface. The incomplete structure of SA is due to clipping. (B) Stereoview showing the enzyme-bound SA molecule and its interactions with the protein and the cofactor. The amino acid residues are shown as stick models in atomic color scheme (C, green; O, red; and N, blue), water molecules as yellow spheres, and the two ligands in distinct colors. Dotted lines in black represent strong electrostatic interactions. For clarity, either main-chain or side-chain atoms are not shown for a few residues.

β12) flanked by three α-helices (α5, α6, and α7) on one side and one α-helix (α8) and two 3_{10} helices on the other side of the sheet. The catalytic domain contains residues 1−105 and 242−269. It also contains a six-stranded β-sheet (β2, β1, β3, β5, β6, and β4; all parallel except β5) and is flanked on each side by three α-helices (α1, α9, and α10; α2, α3, and α4). The two domains are linked to each other by two helices, α5 and α9. A deep groove is formed between the two domains in which the cofactor $NADP^+$ and substrate SA are located (Figure 1B).

Open and Closed Conformations. The root-mean-square deviation (RMSD) between the Cα positions in the eight copies of apo-AaSD ranges from 0.20 to 0.65 Å; comparatively, molecule F is more open than others. The RMSD between the four copies of AaSD·$NADP^+$·SA ranges from 0.32 to 0.81 Å; relatively, molecule D exhibits the most closed conformation with lowest average *B*-factors and best electron density for the ligands. Alignment for individual domains results in much smaller RMSDs.

When molecule F of apo-AaSD and molecule D of AaSD·$NADP^+$·SA are superimposed based on the Cα trace alignment of their NADP-binding domains, a 4.8 Å shift of the loop linking β1 and α1 is observed between the open and the closed conformation of AaSD. Similar shifts are observed for the loop between β2 and α2 and that between β3 and α3 (not shown).

The AaSD·$NADP^+$·SA Structure Represents the Catalytic Complex. In the AaSD·$NADP^+$·SA structure (closed form), the SA and $NADP^+$ are brought into close contact in a sealed cavity; the C3−O3 bond of SA is parallel with the C4−C5 bond of the nicotinamide ring of $NADP^+$, and the distance between the two bonds is 3.5 Å (Figure 2A). In the TtSD·$NADP^+$·SA structure (open form), however, the SA molecule shifts away from $NADP^+$ by ∼1.5 Å, allowing two water molecules to wedge in between the SA and the $NADP^+$ nicotinamide (not shown). Therefore, the TtSD·$NADP^+$·SA structure (PDB entry 2EV9) is not catalytically competent, whereas our AaSD·$NADP^+$·SA structure represents the

catalytic complex, in which atom C3 of the substrate is positioned to donate a hydride to (or to receive a hydride from) atom C4 of the nicotinamide moiety of the cofactor. In spite of that, apparently, the reaction did not occur.

The crystallization of the AaSD·$NADP^+$·SA complex is probably due to the low activity of the enzyme and the equilibrium constant favoring the formation of SA and $NADP^+$, both of which are caused by the low pH. The equilibrium constant ([SA][$NADP^+$]/[DHSA][NADPH]) at 30 °C was determined by Yaniv and Gilvarg (*34*) to be 27.7 at pH 7 and 5.7 at pH 7.8 and by Balinsky and corworkers (*35*) to be 9.25 at pH 7.4. As of any dehydrogenase reaction, the equilibrium position of the AaSD-catalyzed reaction is dependent on the hydrogen ion concentration of the environment. A low pH environment favors the formation of SA and $NADP^+$, whereas a high pH condition favors the formation of DHSA and NADPH (Figure 1A). Thus, the SD-catalyzed oxidation of SA is assayed usually at or near pH 9 (*13*, *14*, *20*, *21*, *36*). In our crystallization experiment, the pH values for the protein and well solution were 7.2 and 4.6, respectively, giving rise to an immediate acidic environment when the two solutions were mixed for crystallization. The pH value in the drops became even lower during the crystallization process because the drop (4 μL volume) was equilibrated with the well solution (1 mL volume) in a closed system. The equilibrium constant at pH 5 is estimated to be ~3000 in favor of the formation of SA and $NADP^+$. The apparent k_{cat} at pH 5 was determined to be 0.22 s^{-1}, which is ~0.36% of that at pH 9 as described in a later section. Thus, in the crystallization mother liquor, $NADP^+$ and SA are the majority species when compared with NADPH and DHSA. The crystallization of the AaSD·$NADP^+$·SA complex further moves the equilibrium in favor of the formation of $NADP^+$ and SA (Figure 1A). Although the geometry of $NADP^+$ is not distinguishable from that of the NADPH at this resolution (Figure 1C), the geometry of SA, characterized by a tetrahedral (sp^3) C3 (Figure 1D), is distinct from that of DHSA, in which the geometry of C3 is planar (sp^2).

Catalytic Center Assembly. The binding of cofactor $NADP^+$ to SD has been previously described in detail in several binary complexes of the enzyme and the cofactor (*13*, *16*, *17*, *19*). Briefly, the backbone amide groups of the P-loop act as donors of hydrogen bonds to the diphosphate and the 3′-hydroxyl of the adenine ribose moiety of $NADP^+$. The loop between β8 and α7 contains two conserved residues, Asn153 and Arg154, which are involved in the binding of the adenosine moiety. The 2′-phosphate is further stabilized by two hydrogen bonds between phosphate oxygen and the guanidinium group of Arg154. The amide group of the nicotinamide forms two hydrogen bonds with main-chain atoms of Ile214 and Gly235. In addition, the ribose interacts with the protein via indirect hydrogen bonds. All of these interactions are observed in the AaSD·$NADP^+$·SA structure, indicating that $NADP^+$ binding is conserved and not significantly altered by the conformational change of the protein. Unlike $NADP^+$, the SA molecule shifts significantly when the protein closes up. In the following sections, the SA binding will be described mainly on the basis of our AaSD·$NADP^+$·SA structure (closed form).

The SA-binding site is a pocket between the central β-sheet of the catalytic domain and the flanking helices α1 and α9, in which the SA molecule is surrounded by α9 and three loops (between β1 and α1, β3 and α3, and β6 and α5, respectively), and the entrance of the pocket is blocked by the nicotinamide moiety of $NADP^+$ (Figure 1B). The carboxylate group of SA is hydrogen-bonded to the hydroxyl groups of Ser19, Ser21, and Tyr216 (Figure 2B). Residues Ser19 and Ser21, highly conserved in the SD family, form two hydrogen bonds with one of the two carboxylate oxygen atoms of SA, while Tyr216 forms a hydrogen bond with the other carboxylate oxygen. Tyr216, also conserved among SD sequences but to a lesser degree, is located in the NADP-binding domain, but its side chain projects into the SA-binding pocket, forming a strong hydrogen bond with the carboxylate group of SA. The three hydroxyl groups of SA interact extensively with the protein (Figures 2B and 4). The C4-hydroxyl forms two hydrogen bonds with the side chains of highly conserved residues Asn91 and Asp106, the C5-hydroxyl forms two hydrogen bonds with Asn64 and Gln242, and the C3-hydroxyl forms two hydrogen bonds with Lys70 and Thr66. Residues Lys70 and Asp106 are highly conserved among SD sequences (*21*); a salt bridge (2.9 Å) is formed between the two side chains.

The stereospecific oxidation (or reduction) of SA (or DHSA) by $NADP^+$ (or NADPH) is known to occur from the A-side of the cofactor (*37*), and during the reaction, atom C3 of the substrate must be positioned to donate (or receive) a hydride to (or from) atom C4 of the nicotinamide ring of the cofactor. From the open to the closed form, three loops in the catalytic domain move toward the NADP-binding domain by ~5 Å and thereby seal the active center of the enzyme. In the AaSD·$NADP^+$·SA structure, the C3−O3 bond of SA is positioned parallel with the C4−C5 bond of the nicotinamide moiety of $NADP^+$ in a close proximity (3.5 Å, Figure 2A). Thus, the C4 of the $NADP^+$ nicotinamide is positioned to receive a hydride from C3 of SA, which is ~2.4 Å away (not shown), in agreement with the theoretically predicted distance (2.2−2.6 Å) for the arrangement of reactants in the liver alcohol dehydrogenase (*38*, *39*).

In the AaSD·$NADP^+$·SA structure, we have identified a water molecule located near the side chains of Lys70 and Asp106 (Figure 2B). It is conserved in all 12 chains of the two structures reported here. It was also observed in 24 out of 33 chains of 13 previously reported SD structures (PDB entries 1NPD, 1O9B, 1NYT, 1NVT, P74, 1P77, 1NPY, 1VI2 1WXD, 2CY0, 2D5C, 2EV9, and 2EZ3). This water molecule is enclosed in a cavity rendered by six residues (Lys70, Ala89, Asn91, Asn104, Gly133, and Ala 137) with optimized electrostatic interactions as well as van der Waals contacts with the protein (Figure 2B). It reaches the C3 oxygen of SA via a proton-conducting wire through the Asp106-Lys70 pair. It also has access to the bulk solvent through either Asn104 or Gly133. Therefore, this water molecule is in position to facilitate proton transfer during the oxidation−reduction reaction.

Biochemical Analysis. The SD activity was measured in the direction of the formation of NADPH and DHSA. Steady-state kinetic parameters were first measured at pH 9.0 for comparison with those of other SDs, because most of the reported kinetic analyses of SDs were carried out at or near this pH (*13*, *14*, *20*, *21*, *36*). The values of the apparent kinetic parameters of AaSD are listed together with those of some bacterial SDs in Table 3. AaSD is rather active for an enzyme from a hyperthermophile that grows best near

Table 3: Apparent Kinetic Parameters of AaSD and Other Bacterial SDs

organism	k_{cat} (s^{-1})	K_m(SA) (μM)	K_m(NADP) (μM)
A. aeolicus[a]	55.5 ± 1.5	42.4 ± 1.6	42.4 ± 0.9
A. fulgidus[b]	390	170	190
E. coli[c]	237	65	58
M. tuberculosis[d]	399	30	63
H. pylori[e]	7.7	148	182

[a] This work and determined at 25 °C and pH 9.0. [b] From ref *42* and determined at 87 °C and pH 7.3. [c] From ref *13* and determined at 20 °C and pH 9.0. [d] From ref *36* and determined at 25 °C and pH 9.0. [e] From ref *41* and determined at 25 °C and pH 8.0.

95 °C (*40*). The k_{cat} of AaSD is comparable to those of mesophilic enzymes from *E. coli* (*13*), *Mycobacterium tuberculosis* (*36*), and *Helicobacter pylori* (*41*). The K_m values for both SA and $NADP^+$ are also comparable to those of the mesophilic enzymes. The SD from another hyperthermophile, *Archaeoglobus fulgidus*, with an optimal growth temperature at 83 °C has been characterized (*42*). Its k_{cat} was determined to be 390 s^{-1} at 87 °C and pH 7.3, and we estimated it to be 2.5 s^{-1} at 25 °C based on the reported activation energy for the enzyme (*42*). For comparison, the k_{cat} of AaSD at 25 °C and pH 7.3 is 22 s^{-1}, which is significantly high than that of the SD from *A. fulgidus*.

To determine the effects of pH on the activity of AaSD, we determined the pH profile of the kinetic parameters for SA at the saturating concentration of $NADP^+$ (1 mM). As mentioned earlier, pH has dramatic effects on the activity of the enzyme. The k_{cat} of AaSD at pH 5 is only ~0.36% of that at pH 9. The k_{cat}−pH profile (Figure 3A) is characteristic of an enzyme with a residue that functions as a general base for catalysis. The apparent pK_a estimated from the kinetic measurements was 7.5 ± 0.1. On the basis of the structure described earlier, the residue that most likely functions as a general base is Lys70. The apparent pK_a value is similar to that (8.1) of the corresponding lysine residue in *Haemophilus influenza* SD-L estimated from a similar pH profile (*14*) but is significantly different from that (8.9) of the corresponding lysine residue in *M. tuberculosis* SD obtained for the reverse reaction (i.e., the formation of SA and $NADP^+$) (*43*). It is not clear at present whether the differences in the apparent pK_a values are caused by the local environments of the lysine or the different degrees of the "stickness" of the substrate relative to catalytic turnover.

The k_{cat}/K_m−pH profile (Figure 3B), different from the k_{cat}−pH profile (Figure 3A), is characteristic for those of two ionizable groups, one of which needs to be deprotonated and the other needs to be protonated for optimal activity. The apparent pK_a values were estimated to be 6.7 ± 0.1 and 9.7 ± 0.1, respectively, by nonlinear regression analysis as described in the Experimental Procedures section. The residue with a pK_a of 6.7 could be either Lys70 or Asp106 based on the structure as both residues are hydrogen bonded to SA. Alternatively, this apparent pK_a value may reflect the effects of the ionization of both residues on the binding of SA and/or subsequent catalysis. The residue with a pK_a of 9.7 is most likely Tyr216, which is hydrogen bonded to the carboxyl group of SA. When the phenolyl group of Tyr216 is deprotonated, it is expected to decrease the affinity of the enzyme for SA significantly.

Proposed Mechanism. On the basis of our structural and biochemical analyses described here and those reported by

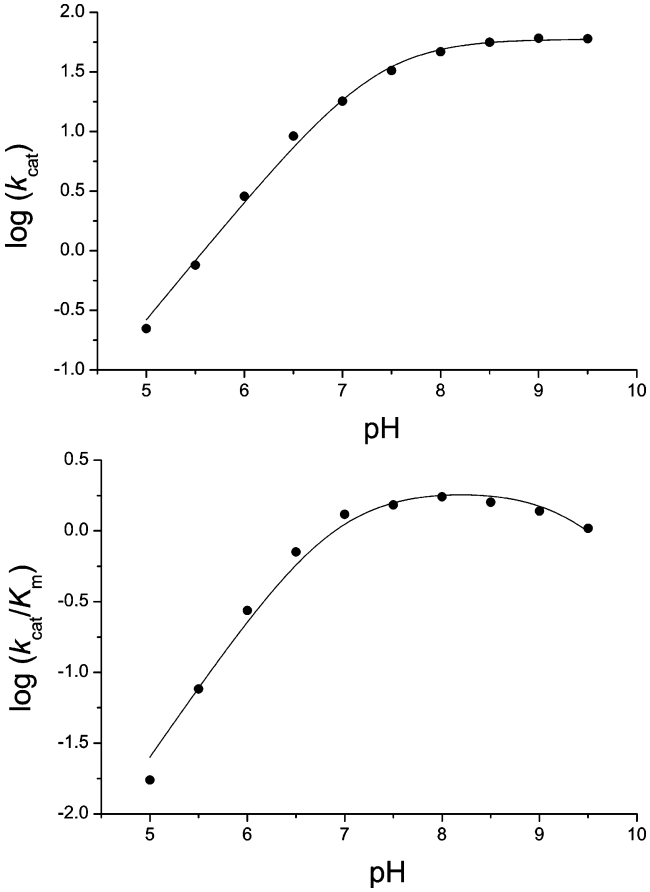

FIGURE 3: log(k_{cat})−pH (A) and log(k_{cat}/K_m)−pH (B) profiles of AaSD. The solid lines were obtained by nonlinear regression as described in the Experimental Procedures section.

others, we propose a catalytic mechanism for AaSD as depicted in Figure 4. The active enzyme for the dehydrogenation of SA (Figure 4A) contains a deprotonated lysine (Lys70), a deprotonated aspartate (Asp106), and a protonated tyrosine (Tyr216). The hydride transfer and the deprotonation of the 3-hydroxyl group of SA are suggested to proceed in a concerted manner based on the measurements of kinetic isotope effects on the *M. tuberculosis* SD-catalyzed reaction (*43*). Lys70 functions as a general base and becomes protonated in the dehydrogenation reaction (Figure 4B). The proton is then transferred to the bulk solvent via the short proton-conducting wire. Although the proposed mechanism of proton transfer is depicted as a stepwise process in Figure 4, it can be a concerted process. In either case, Asp106 plays a critical role in the transfer of a proton to the bulk solvent.

While the three types of SDs (AroE, YdiB, and SD-L) have the same fold, their active centers are significantly different. Although they all can catalyze the SD reaction, the SD reaction may be only a side activity for YdiB and SD-L, with a reported k_{cat} of ~0.1 s^{-1} for *E. coli* YdiB (*21*) and 0.2 s^{-1} for *H. influenza* SD-L (*14*). YdiB can catalyze the dehydrogenation of quinate and is believed to be involved in quinate catabolism (*13*) or a branch point enzyme for quinate biosynthesis from the shikimate pathway (*14*). Furthermore, unlike AroE and SD-L, which use exclusively NADP as their cofactor, YdiB prefers NAD to NADP for the dehydrogenation of both quinate and shikimate (*13*). On the basis of the structural comparison of *E. coli* AroE and YdiB, the NAD preference of YdiB is attributed to the

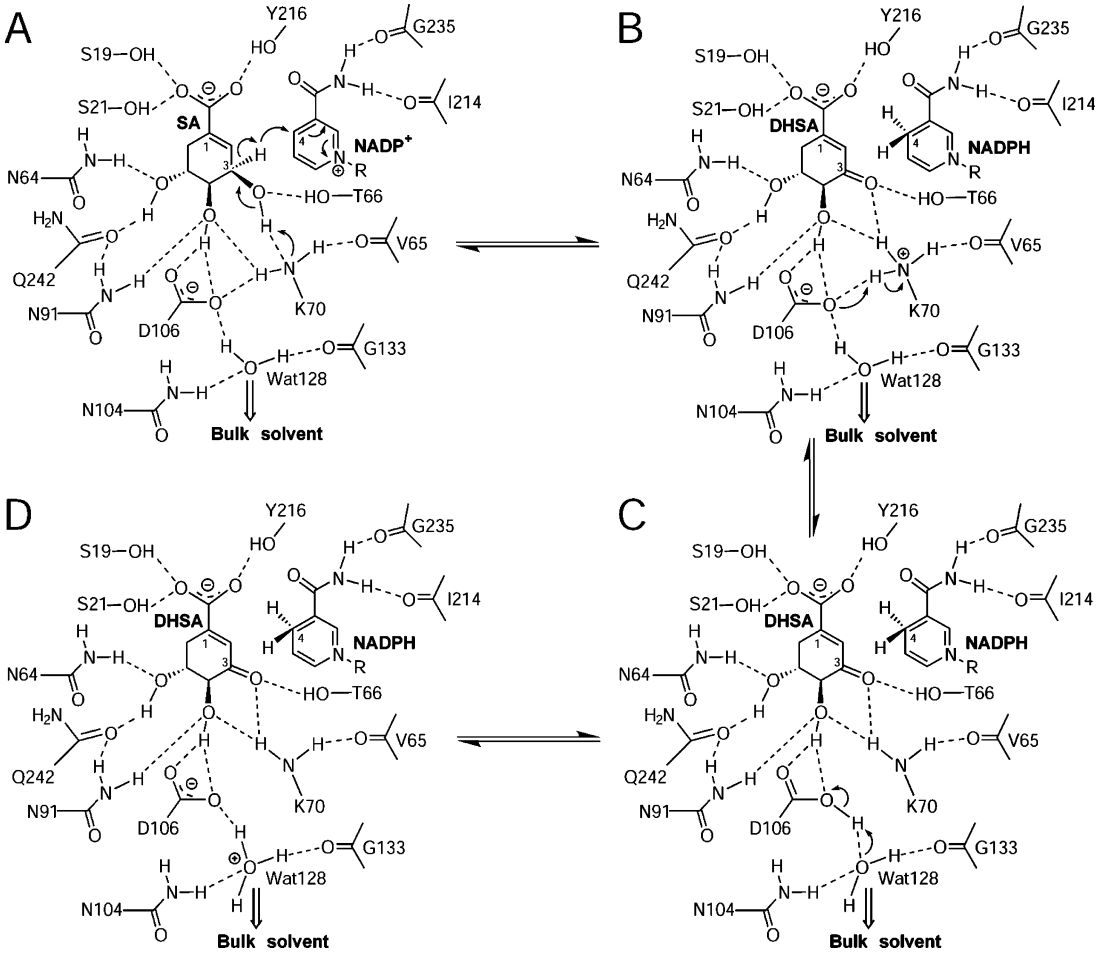

FIGURE 4: Proposed catalytic mechanism for AaSD. Only polar residues that interact with SA and the nicotinamide moiety of $NADP^+$ are shown. Hydrogen bonds are indicated by dashed lines and electron flows by curved arrows. The hydride transfer is concerted with the deprotonation of the 3-hydroxyl group of SA (A to B). The proton transfer from Lys70 to the bulk solvent is proposed to be facilitated by Asp106 (C and D).

substitution of T151 and R154 in AroE by D158 and F160 in YdiB, respectively (*13*). The biological function of SD-L is not known at present, but it is believed to be involved in a new branch from the shikimate pathway (*14*). The low SD activities of YdiB and SD-L are caused by active site residue substitutions, but a more precise description has to wait until the structures of YdiB and SD-L in complex with shkimate are determined. The substitutions not only cause the exchange of functional groups of the substituted residues but also may alter the function of the conserved residues because of the repositioning of their side chains as a consequence of the substitution of other residues. For example, R150 in AroE corresponds to R158 in YdiB, and the residue is conserved between the two enzymes, but the position of the guanidinium group of R150 in AroE is significantly different from that of R158 in YdiB. Consequently, the guanidinium group of R150 in AroE forms two hydrogen bonds with the 2′-phosphate, but the guanidinium group of R158 in YdiB is not in a position to interact with the ribose moiety of NAD. Similarly, the positions of the conserved aspartate and lysine residues relative to the bound shikimate may be different among AroE, YdiB, and SD-L and consequently have different functions. Thus, substitution of the conserved lysine residue (Lys71) in *E. coli* YdiB with Ala caused only a decrease in k_{cat} by a factor of 8 but an increase in K_m for SA by a factor of 180 (*21*). Surprisingly, substitution of the corresponding aspartate residue (Asp107) in YdiB with Ala caused a small increase in k_{cat} but a dramatic decrease in K_m for SA (by a factor of 1.4×10^4). For both mutations, the K_m values for NAD are similar to that of the wild-type YdiB. Although the rate constants for individual steps are not known for any SD, the chemical step is most likely rate-limiting for the YdiB-catalyzed SA dehydrogenation reaction, because its k_{cat} value for the reaction is extremely low (*21*). The results taken together strongly suggest that (1) the conserved lysine residue in YdiB plays only a minor role in catalysis and is more important for the binding of SA and (2) the conserved aspartate residue is critically important for the binding of SA but is not important for catalysis. In contrast, substitution of the corresponding lysine residue (Lys385) in the *Arabidopsis* dehydroquinate dehydratase−shikimate dehydrogenase with Ala resulted in a decrease in k_{cat} by a factor of 3.3×10^4 and a decrease in K_m by about 2-fold, suggesting that the lysine residue plays a critical role in catalysis. Substitution of the corresponding aspartate residue (Asp423) with Asn caused a decrease in k_{cat} by a factor of 3.5×10^3 and essentially no change in K_m. However, the carboxamide of the asparagine residue may be able to maintain the hydrogen bond with the 4-hydroxyl group of SA. When the aspartate residue was substituted with Ala, the mutation rendered an enzyme with no measurable activity, suggesting that the aspartate residue is also critically

important for catalysis. The site-directed mutagenesis studies of the *Arabidopsis* enzyme also suggests that the deprotonation of the 3-hydroxyl group of SA plays a major role in the oxidation of SA. Mutagenesis studies of the conserved aspartate and lysine residues in *H. influenza* SD-L also indicate that the two residues are critical for its SD activity. On the basis of the crystal structures reported in this paper, we suggest that Lys70 in AaSD plays mainly a catalytic role as a general base for the deprotonation of the 3-hydroxyl group of SA in the oxidation of SA. Asp106 is important for both the binding of SA and the catalysis as a mediator for the proton transfer from Lys70 to the bulk solvent. The proposed functional roles of these important residues await site-directed mutagenesis and biochemical studies.

ACKNOWLEDGMENT

We thank Zbigniew Dauter, John J. Chrzas, and Zhongmin Jin for help during data collection. X-ray diffraction data were collected at the X9B beamline of the National Synchrotron Light Source, Brookhaven National Laboratory, and the SER-CAT 22-ID beamline of the Advanced Photon Source, Argonne National Laboratory. Supporting institutions may be found at www.ser-cat.org/members.html.

REFERENCES

1. Bentley, R. (1990) The shikimate pathway—a metabolic tree with many branches, *Crit. Rev. Biochem. Mol. Biol. 25*, 307−384.
2. Haslam, E. (1993) *Shikimic Acid: Metabolism and Metabolites*, John Wiley & Sons, Chichester.
3. Kishore, G. M., and Shah, D. M. (1988) Amino acid biosynthesis inhibitors as herbicides, *Annu. Rev. Biochem. 57*, 627−663.
4. Davies, G. M., Barrett-Bee, K. J., Jude, D. A., Lehan, M., Nichols, W. W., Pinder, P. E., Thain, J. L., Watkins, W. J., and Wilson, R. G. (1994) (6*S*)-6-fluoroshikimic acid, an antibacterial agent acting on the aromatic biosynthetic pathway, *Antimicrob. Agents Chemother. 38*, 403−406.
5. Coggins, J. R. (1989) The shikimate pathway as a target for herbicides, in *Herbicides and Plant Metabolism* (Dodge, A., Ed.) pp 97−112, Cambridge University Press, Cambridge, U.K.
6. Roberts, F., Roberts, C. W., Johnson, J. J., Kyle, D. E., Krell, T., Coggins, J. R., Coombs, G. H., Milhous, W. K., Tzipori, S., Ferguson, D. J., Chakrabarti, D., and McLeod, R. (1998) Evidence for the shikimate pathway in apicomplexan parasites, *Nature 393*, 801−805.
7. Ridley, R. G. (1998) Planting new targets for antiparasitic drugs, *Nature Med. 4*, 894−895.
8. Knop, D. R., Draths, K. M., Chandran, S. S., Barker, J. L., von Daeniken, R., Weber, W., and Frost, J. W. (2001) Hydroaromatic equilibration during biosynthesis of shikimic acid, *J. Am. Chem. Soc. 123*, 10173−10182.
9. Ran, N., Knop, D. R., Draths, K. M., and Frost, J. W. (2001) Benzene-free synthesis of hydroquinone, *J. Am. Chem. Soc. 123*, 10927−10934.
10. Steinrucken, H. C., and Amrhein, N. (1980) The herbicide glyphosate is a potent inhibitor of 5-enolpyruvyl-shikimic acid-3-phosphate synthase, *Biochem. Biophys. Res. Commun. 94*, 1207−1212.
11. Lee, L. J., and Ngim, J. (2000) A first report of glyphosate-resistant goosegrass (*Eleusine indica* (L) Gaertn) in Malaysia, *Pest Manage. Sci. 56*, 336−339.
12. Heap, I. M. (1999) The occurrence of herbicide-resistant weeds worldwide, *Pestic. Sci. 51*, 235−243.
13. Michel, G., Roszak, A. W., Sauve, V., Maclean, J., Matte, A., Coggins, J. R., Cygler, M., and Lapthorn, A. J. (2003) Structures of shikimate dehydrogenase AroE and its paralog YdiB. A common structural framework for different activities, *J. Biol. Chem. 278*, 19463−19472.
14. Singh, S., Korolev, S., Koroleva, O., Zarembinski, T., Collart, F., Joachimiak, A., and Christendat, D. (2005) Crystal structure of a novel shikimate dehydrogenase from *Haemophilus influenzae*, *J. Biol. Chem. 280*, 17101−17108.
15. Berman, H. M., Westbrook, J., Feng, Z., Gilliland, G., Bhat, T. N., Weissig, H., Shindyalov, I. N., and Bourne, P. E. (2000) The Protein Data Bank, *Nucleic Acids Res. 28*, 235−242.
16. Benach, J., Lee, I., Edstrom, W., Kuzin, A. P., Chiang, Y., Acton, T. B., Montelione, G. T., and Hunt, J. F. (2003) The 2.3-Å crystal structure of the shikimate 5-dehydrogenase orthologue YdiB from *Escherichia coli* suggests a novel catalytic environment for an NAD-dependent dehydrogenase, *J. Biol. Chem. 278*, 19176−19182.
17. Padyana, A. K., and Burley, S. K. (2003) Crystal structure of shikimate 5-dehydrogenase (SDH) bound to NADP: insights into function and evolution, *Structure 11*, 1005−1013.
18. Ye, S., Von Delft, F., Brooun, A., Knuth, M. W., Swanson, R. V., and McRee, D. E. (2003) The crystal structure of shikimate dehydrogenase (AroE) reveals a unique NADPH binding mode, *J. Bacteriol. 185*, 4144−4151.
19. Badger, J., Sauder, J. M., Adams, J. M., Antonysamy, S., Bain, K., Bergseid, M. G., Buchanan, S. G., Buchanan, M. D., Batiyenko, Y., Christopher, J. A., Emtage, S., Eroshkina, A., Feil, I., Furlong, E. B., Gajiwala, K. S., Gao, X., He, D., Hendle, J., Huber, A., Hoda, K., Kearins, P., Kissinger, C., Laubert, B., Lewis, H. A., Lin, J., Loomis, K., Lorimer, D., Louie, G., Maletic, M., Marsh, C. D., Miller, I., Molinari, J., Muller-Dieckmann, H. J., Newman, J. M., Noland, B. W., Pagarigan, B., Park, F., Peat, T. S., Post, K. W., Radojicic, S., Ramos, A., Romero, R., Rutter, M. E., Sanderson, W. E., Schwinn, K. D., Tresser, J., Winhoven, J., Wright, T. A., Wu, L., Xu, J., and Harris, T. J. (2005) Structural analysis of a set of proteins resulting from a bacterial genomics project, *Proteins: Struct., Funct., Genet. 60*, 787−796.
20. Singh, S. A., and Christendat, D. (2006) Structure of *Arabidopsis* dehydroquinate dehydratase-shikimate dehydrogenase and implications for metabolic channeling in the shikimate pathway, *Biochemistry 45*, 7787−7796.
21. Lindner, H. A., Nadeau, G., Matte, A., Michel, G., Menard, R., and Cygler, M. (2005) Site-directed mutagenesis of the active site region in the quinate/shikimate 5-dehydrogenase YdiB of *Escherichia coli*, *J. Biol. Chem. 280*, 7162−7169.
22. Ji, X., Blaszczyk, J., and Chen, X. (2001) The absorption edge of protein-bound mercury and a double-edge strategy for HgMAD data acquisition, *Acta Crystallogr. D 57*, 1003−1007.
23. Otwinowski, Z., and Minor, W. (1997) Processing of X-ray diffraction data collected in oscillation mode, *Methods Enzymol. 276*, 307−326.
24. Collaborative Computational Project Number 4 (1994) The CCP4 Suite: Programs for Protein Crystallography, *Acta Crystallogr. D 50*, 760−763.
25. Terwilliger, T. C., and Berendzen, J. (1999) Automated MAD and MIR structure solution, *Acta Crystallogr. D 55*, 849−861.
26. de La Fortelle, E., and Bricogne, G. (1997) Maximum-likelihood heavy-atom parameter refinement for multiple isomorphous replacement and multiwavelength anomalous diffraction methods, *Methods Enzymol. 276*, 472−494.
27. Reed, R. J. (2000) Pushing the boundaries of molecular replacement with maximum likelihood, *Acta Crystallogr. D 57*, 1373−1382.
28. Brünger, A. T., Adams, P. D., Clore, G. M., DeLano, W. L., Gros, P., Grosse-Kunstleve, R. W., Jiang, J. S., Kuszewski, J., Nilges, M., Pannu, N. S., Read, R. J., Rice, L. M., Simonson, T., and Warren, G. L. (1998) Crystallography & NMR system: A new software suite for macromolecular structure determination, *Acta Crystallogr. D 54*, 905−921.
29. Jones, T. A., and Kjeldgaard, M. (1997) Electron-density map interpretation, *Methods Enzymol. 277*, 173−208.
30. Laskowski, R. A., MacArthur, M. W., Moss, D. S., and Thornton, J. M. (1993) PROCHECK: a program to check stereochemical quality of protein structures, *J. Appl. Crystallogr. 26*, 283−291.
31. Vriend, G. (1990) WHAT IF: a molecular modeling and drug design program, *J. Mol. Graphics 8*, 52−56, 29.
32. Kraulis, P. J. (1991) MOLSCRIPT: a program to produce both detailed and schematic plots of protein structures, *J. Appl. Crystallogr. 24*, 946−950.
33. DeLano, W. L. (2002) Delano Scientific, San Carlos, CA.
34. Yaniv, H., and Gilvarg, C. (1955) Aromatic biosynthesis. XIV. 5-Dehydroshikimic reductase, *J. Biol. Chem. 213*, 787−795.
35. Balinsky, D., Dennis, A. W., and Cleland, W. W. (1971) Kinetic and isotope-exchange studies on shikimate dehydrogenase from *Pisum sativum*, *Biochemistry 10*, 1947−1952.
36. Zhang, X., Zhang, S., Hao, F., Lai, X., Yu, H., Huang, Y., and Wang, H. (2005) Expression, purification and properties of

shikimate dehydrogenase from *Mycobacterium tuberculosis*, *J. Biochem. Mol. Biol. 38*, 624−631.
37. Dansette, P., and Azerad, R. (1973) The shikimate pathway. I. Preparation of 3-^{3}H, 4-^{3}H and 2,4-$^{3}H_2$ D-shikimic acid, *Biochimie 55*, 583−589.
38. Cui, Q., Elstner, M., and Karplus, M. (2002) A theoretical analysis of the proteon and hidride transfer in liver alcohol dehdrogenase (LADH), *J. Phys. Chem. B 106*, 2721−2704.
39. Agarwal, P. K., Webb, S. P., and Hammes-Schiffer, S. (2000) Computational studies of the mechanism for proton and hudride transfer inliver alcohol dehydrogenase, *J. Am. Chem. Soc. 122*, 4803−4812.
40. Deckert, G., Warren, P. V., Gaasterland, T., Young, W. G., Lenox, A. L., Graham, D. E., Overbeek, R., Snead, M. A., Keller, M., Aujay, M., Huber, R., Feldman, R. A., Short, J. M., Olsen, G. J., and Swanson, R. V. (1998) The complete genome of the hyperthermophilic bacterium *Aquifex aeolicus*, *Nature 392*, 353−3538.
41. Han, C., Wang, L., Yu, K., Chen, L., Hu, L., Chen, K., Jiang, H., and Shen, X. (2006) Biochemical characterization and inhibitor discovery of shikimate dehydrogenase from *Helicobacter pylori*, *FEBS J. 273*, 4682−4692.
42. Lim, S., Schroder, I., and Monbouquette, H. G. (2004) A thermostable shikimate 5-dehydrogenase from the archaeon *Archaeoglobus fulgidus*, *FEMS Microbiol. Lett. 238*, 101−106.
43. Fonseca, I. O., Silva, R. G., Fernandes, C. L., de Souza, O. N., Basso, L. A., and Santos, D. S. (2007) Kinetic and chemical mechanisms of shikimate dehydrogenase from *Mycobacterium tuberculosis*, *Arch. Biochem. Biophys. 457*, 123−133.

BI602601E